Origin of the weakly temperature-dependent thermal conductivity in ZIF-4 and ZIF-62

Yanguang Zhou, Yixin Xu, Yufei Gao, Sebastian Volz

Origin of the weakly temperature-dependent thermal conductivity in ZIF-4 and ZIF-62

Yanguang Zhou,[1,*] Yixin Xu,[1] Yufei Gao,[2] and Sebastian Volz[3]

[1]*Department of Mechanical and Aerospace Engineering, The Hong Kong University of Science and Technology, Clear Water Bay, Kowloon, Hong Kong SAR*

[2]*Key Laboratory of Ocean Energy Utilization and Energy Conservation of Ministry of Education, School of Energy and Power Engineering, Dalian University of Technology, Dalian, China*

[3]*LIMMS/CNRS-IIS(UMI2820) Institute of Industrial Science, University of Tokyo 4-6-1 Komaba, Meguro-ku Tokyo, 153-8505, Japan*

(Received 8 May 2021; revised 26 November 2021; accepted 7 January 2022; published 24 January 2022)

It is known that the temperature-dependent thermal conductivity of conventional crystals follows the classical $1/T$ trend due to the dominant umklapp phonon-phonon scattering at high enough temperatures. However, the thermal conductivity of many crystalline metal-organic frameworks is very low and shows a weak temperature dependence when all the vibrational modes are occupied. By studying two metal-organic frameworks, i.e., zeolitic imidazolate framework-4 (ZIF-4) and crystal zeolitic imidazolate framework-62 (ZIF-62), we computationally prove that the ultralow thermal conductivity in ZIF-4 and ZIF-62 is resulting from the strong scattering among the vibrations due to the large mass difference between the metal atom and the organic sites and the large diffusion of organic sites. Unlike only propagating vibrational modes, i.e., phonons, existing in the conventional crystalline Si, our mean free path spectrum analysis uncovers that both propagating and nonpropagating anharmonic vibrational modes exist and contribute largely to thermal conductivity in ZIF-4 and ZIF-62. The obtained weak temperature dependence of thermal conductivity is found to stem from the temperature dependencies of those two kinds of vibrations. Our study provides a fundamental understanding of thermal transport in metal-organic frameworks and will guide the design of thermal-related applications, e.g., inflammable gas storage, chemical catalysis, and solar thermal conversion.

DOI: 10.1103/PhysRevMaterials.6.015403

I. INTRODUCTION

Metal-organic frameworks (MOFs), which are characterized by metal ions or clusters connected by organic bridges [1–4], have attracted intensive attention in the applications of gas storage [5], gas separation [6], and catalysis [7] due to their extremely high porosity and internal surfaces areas. One important and often neglected challenge related to the gas storage in MOFs is the heat generation during the gas adsorption process, which causes a reduction of the gas adsorption capacity [8,9] and even accidents, e.g., hazardous gases leakage [10,11] or risk of explosion [12]. It has been known that the heat generated during the gas adsorption process dissipated through the MOF frameworks is important and deserves additional scrutiny [13]. An in-depth understanding of heat transfer in MOFs is therefore crucial for optimizing their thermal design [8,9,13–22]. Unlike the thermal transport properties of many crystals, e.g., crystalline Si (cSi) [23,24], crystalline Ge [23], and bulk diamond [25], which have been thoroughly investigated, heat transfer mechanisms in MOF crystals may be not based on the same phenomenology (e.g., only inelastic scattering among phonons) and remain poorly documented. For example, both experiments [22] and simulations [21] show that the thermal conductivity of MOF-5 has a weakly positive power-law temperature dependence of $T^{0.13}$. The authors of those studies invoke the concept of dual thermal transport channels including the contributions from both the anharmonic propagating and the harmonic nonpropagating vibrational modes which are depicted by the Cahill-Pohl model [26]. Following another direction, Zhang *et. al.* [20] argue that the weak positive temperature dependence of the thermal conductivity in another MOF, i.e., zeolitic imidazolate framework (ZIF)-8, is stemming from an enhanced overlap in the vibrational density of states (VDOS) between Zn and N atoms, which is itself resulting from the overlap of trajectories between Zn and N atoms. Nevertheless, all these studies rely on the fact that the concept of phonons is still valid in MOFs. Despite these deductions, directly quantifying the scattering mechanisms of the vibrations, e.g., the vibrational mean free path and the thermal conductivity contributed from various types of heat carriers, is still lacking.

In this paper, the thermal transport properties in ZIF-4 and ZIF-62 are quantitatively analyzed, using atomistic simulations. For comparison, we also investigate the thermal transport mechanisms in cSi. Our analysis supports that, unlike only the propagating modes existing in conventional cSi, both propagating and nonpropagating anharmonic vibrational modes exist in ZIF-4 and ZIF-62 and contribute largely to thermal energy transport. The vibrations in ZIF-4 and ZIF-62 are scattered strongly when they transfer thermal energy from the organic sites to the metal atoms because of their large mass difference. Meanwhile, the thermal conductivity of ZIF-4 and ZIF-62 is found to hold a weak or even glasslike temperature dependence which is stemming from the strong scattering among vibrations caused by the large mass difference between metal atoms and organic sites and the large diffusion of the organic sites. We further find the

*Corresponding author: maeygzhou@ust.hk

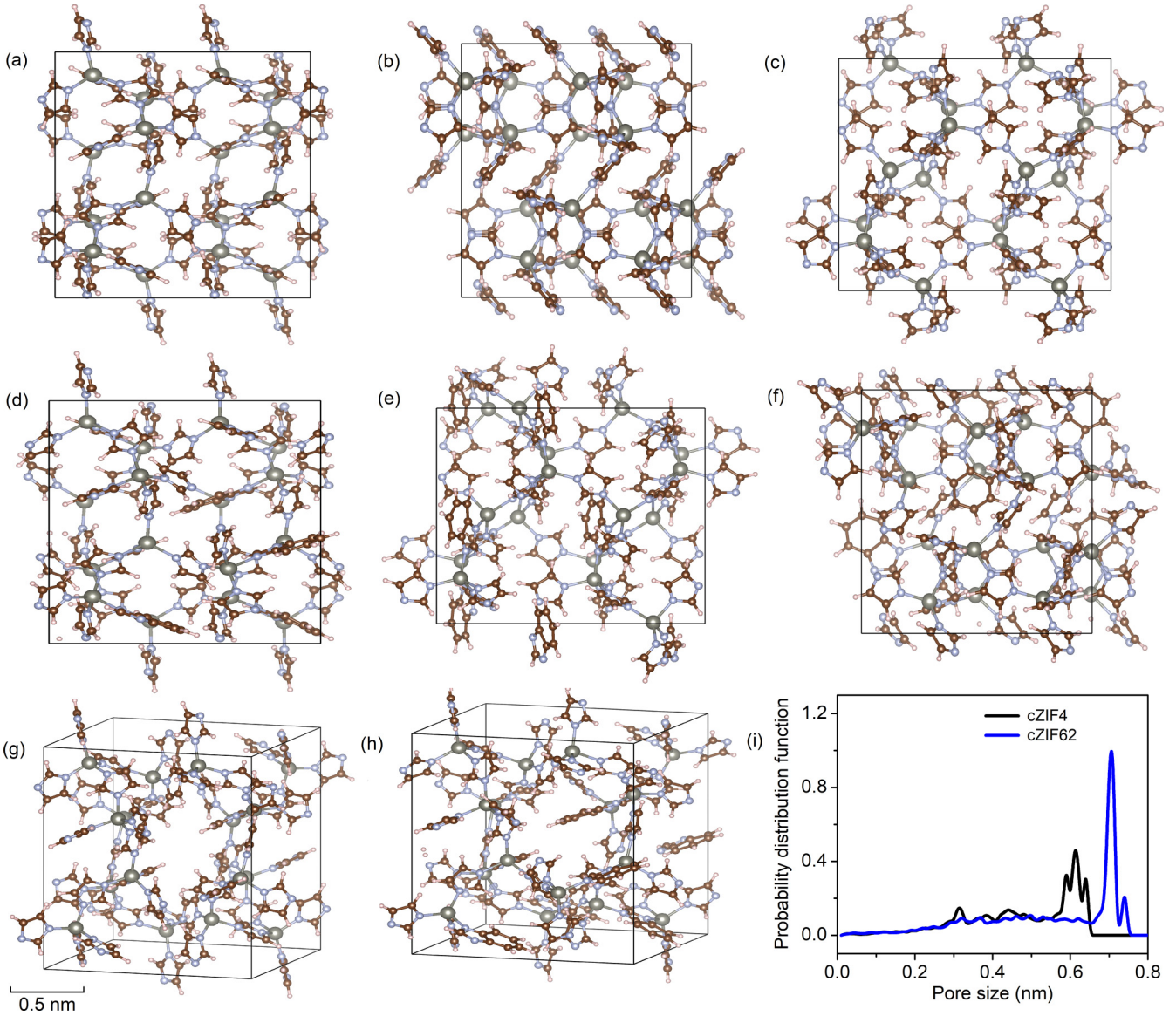

FIG. 1. Unit cell of ZIF-4 in a front view (a), side view (b), and top view (c). The front view (d), side view (e), and top view (f) of ZIF-62. The perspective view of ZIF-4 (g) and ZIF-62 (h). Big gray atoms are Zn, light blue atoms are N, purple atoms are C atoms, and pink atoms are H atoms. (i) Pore size distribution of ZIF-4 and ZIF-62

thermal conductivity contributed by the propagating modes is decreasing with temperature due to the enhanced scattering among vibrations, while the thermal conductivity contributed by the nonpropagating vibrations is found to increase with temperature. The enhancing overlap of the vibrational density of states of these nonpropagating vibrations in 0.2–0.3 and 0.5–0.8 THz (1.0–2.0 THz) for ZIF-4 (ZIF-62) induced by temperature may be the reason.

II. COMPUTATIONAL DETAILS

A. Structure of ZIF-4 and ZIF-62

For ZIF-4 and ZIF-62 which are downloaded from the Crystallography Open Database (COD) [27], each Zn^{2+} atom forms a tetrahedron via linking to four nitrogen atoms of the organic groups [Figs. 1(a)–1(h)]. The density of ZIF-4 and ZIF-62 calculated after the *NPT* (constant particle number, pressure, and temperature) relaxation, is 1.20 and 1.18 g/cm^3, respectively. The density of ZIF-4 here is slightly lower than the crystallographic density of 1.22 g/cm^3 [28] and other reported values of 1.28 g/cm^3 [29] and 1.25 g/cm^3 [28]. The difference between our values and other existing results may be because (i) our simulations are implemented in an environment with standard atmospheric pressure, (ii) the effect of temperature and the classical potential in our simulations, and (iii) the different resources to obtain the initial structures (e.g., the COD for this paper and the Cambridge Structural Database for Ref. [29]). We also calculate the distribution of the pore size in ZIFs, and find that the pore size in ZIF-62 is larger than that in ZIF-4 [Fig. 1(i)] [30]. The porosity of ZIF-4 and ZIF-62 is analyzed using the software POROSITYPLUS [30], which uses the Monte Carlo integration-based method to compute the accessibility to arbitrary probe sizes. To determine the porosity of ZIF-4 and ZIF-62, a probe particle with a radius of 0.1 nm

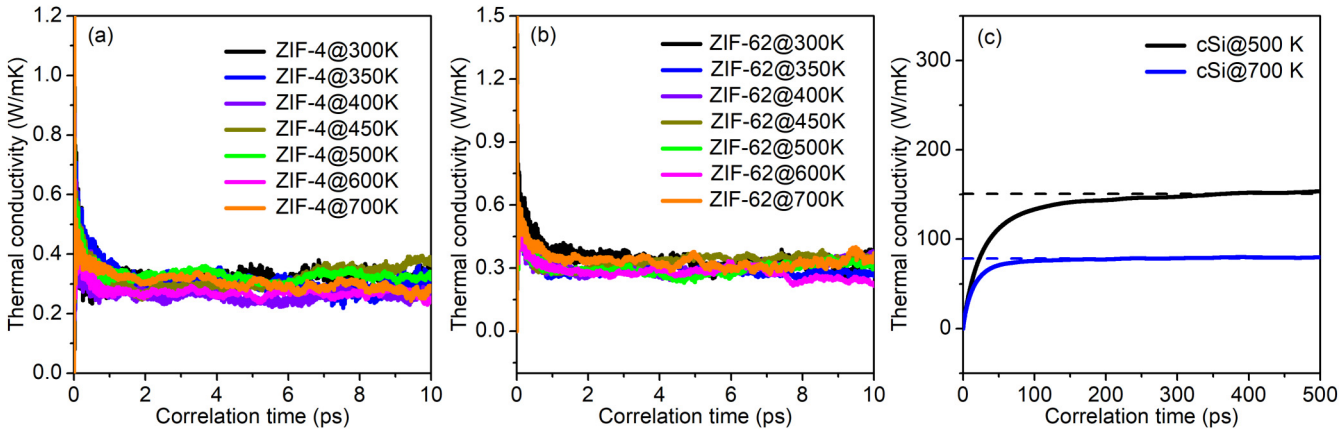

FIG. 2. The time dependent thermal conductivity of (a) ZIF-4 and (b) ZIF-62 with a 3 × 3 × 3 supercell, and (c) crystalline silicon (cSi) at different temperatures.

is inserted into the model at a random position and is checked to ensure that it does not overlap any atoms. If it does not, the insertion is accepted and the fraction of accepted moves to total attempted moves is the value of porosity or volume fraction [30].

B. Green-Kubo equilibrium molecular dynamics simulations

The 3 × 3 × 3 supercell for our crystalline ZIFs and a 6 × 6 × 6 supercell for cSi have large enough sizes to obtain the converged thermal conductivities [21,31], and are first equilibrated at 300–800 K for 125 ps (500 ps) in the *NVT* to reduce the metastabilities. The interactions among the atoms for ZIFs and cSi are depicted using the reactive force field (ReaxFF) potential [32] and Tersoff potential [29], respectively. The heat current of the next 10 ps (500 ps) with a sampling interval of 0.5 fs (2 fs) in the *NVE* (constant particle number, volume and energy) ensemble is used to calculate the thermal conductivity of ZIFs (cSi). The time step in all our simulations is 0.25 fs (1 fs), and periodic boundary conditions were applied in all three directions. The heat current $\vec{Q}$ used to calculate the thermal transport is computed via [33]

$$\vec{Q} \approx -\sum_i \vec{\vec{S}}_i \cdot \vec{v}_i, \tag{1}$$

where $\vec{v}_i$ refers to the atomic velocity, and $\vec{\vec{S}}_i$ is the symmetric stress tensor of atom i. The detailed expression of $\vec{\vec{S}}_i$ can be found in Ref. [20]. Therefore, thermal conductivity κ can be accessed based on the Green-Kubo theory [34]:

$$\kappa = \frac{1}{3k_bVT^2}\int_0^\infty \langle \vec{Q}(t)\cdot\vec{Q}(0)\rangle dt, \tag{2}$$

in which k_b is the Boltzmann constant, V is the system volume, T is the system temperature, and t denotes the autocorrelation time. The angular bracket indicates ensemble averaging. For each case, 20 independent runs are performed to obtain a stable averaged κ. The correlation time considered in our simulation is 10 ps (200 ps), which is long enough to obtain the converged thermal conductivity (Fig. 2). The method used to calculate thermal conductivity is then named Green-Kubo equilibrium molecular dynamics (GKEMD). All the molecular dynamics simulations are performed using LAMMPS [35]. The lattice constants in our molecular dynamical simulations for ZIF-4, ZIF-62, and cSi at 300 K are 1.52, 1.65, and 0.5442 nm, respectively.

C. Nonequilibrium molecular dynamics simulations

The frequency-dependent vibrational information, e.g., vibrational mean free path, is calculated using spectral heat current analysis based on the nonequilibrium molecular dynamics (NEMD) simulations. For the NEMD simulations, fixed boundary conditions are applied to both ends of the system. The periodic boundary conditions are applied in the two in-section directions, whereas the free boundary condition is used in the cross-section direction. To establish a steady heat flux, the top and bottom two layers of atoms with a thickness of 1 nm each in the cross-section direction are considered as the heat source and sink, respectively. The kinetic energy between these two layers is exchanged every 20 time steps following the Muller-Plathe algorithm [36]. A steady temperature gradient is going to be established along the concerned direction (x direction in our simulations) after running the NEMD simulations for 300 ps; the next 50-ps atomic velocity and trajectory will be used for the spectral heat current analysis [37–41]. In this method, the spectral heat current is calculated via

$$Q(\omega) = \sum_{i\in\text{Left}}\sum_{j\in\text{Right}} 2\text{Re}\left[\int_{-\infty}^{+\infty}\left\langle k_{ij}^{\alpha\beta}u_j^\beta(\tau)v_i^\alpha(0)\right\rangle e^{i\omega\tau}d\tau\right], \tag{3}$$

where $\boldsymbol{\kappa}_{ij}^{\alpha\beta}$ is the second-order force constant between the atom i and j along the $\alpha\beta$ direction. v_i and u_j are the atomistic velocity and position, respectively. "Left" and "Right" in Eq. (3) are regarded as the left and right sides of an imaginary interface, respectively. The computational details of spectral heat current analysis can be also found in Ref. [38]. Based on the Landauer theory [42], the phenomenological mean free path (MFP) can be calculated via [43,44]

$$\Lambda(\omega) = \frac{[Q(\omega)\cdot L]/T}{Q_{\text{ballistic}}(\omega)/T_{\text{ballistic}} - Q(\omega)/T}, \tag{4}$$

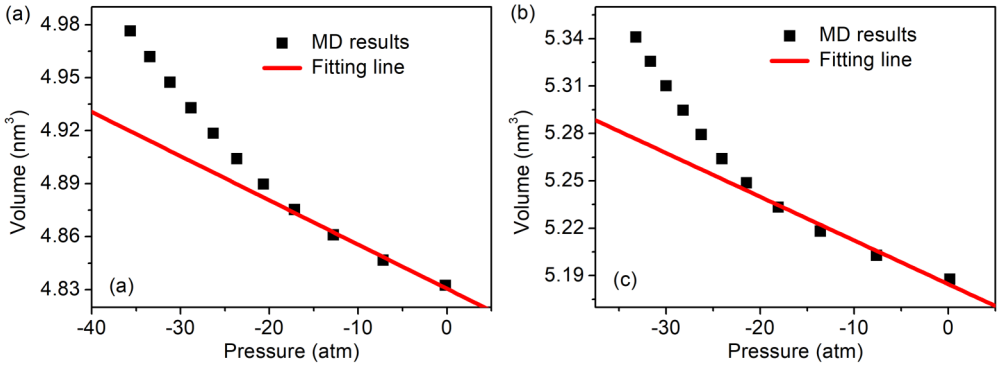

FIG. 3. The volume vs pressure for (a) ZIF-4 and (b) ZIF-62. The black dots are molecular dynamics (MD) simulations results, and the red lines are the fitting lines.

in which T is the temperature gradient and L is the length of the system. $Q_{\text{ballistic}}(\omega)$ and $T_{\text{ballistic}}$ are the ballistic heat current and ballistic temperature gradient, respectively. The size of the system used to calculate the ballistic heat current $Q_{\text{ballistic}}(\omega)$ is around 0.8 nm which is around half of the lattice constant. The corresponding temperature in this system is called the ballistic temperature gradient $T_{\text{ballistic}}$. For ZIF-4 and ZIF-62, we choose $L = 12$ nm for the spectral MFP calculations, which is long enough to eliminate the size effect as the MFP is smaller than 2 nm. We note that the phenomenological MFP may be smaller than the length of the Zn-N bond and therefore is ill-defined. These MFPs smaller than the length of the Zn-N bond do not have physical meanings and can be mathematically represented by $[3D(\omega)\tau(\omega)]^{1/2}$ [45], in which $D(\omega)$ is the diffusivity and $\tau(\omega)$ is the relaxation time. For cSi, these vibrations with the mean free path larger than 220 nm cannot be included since the length of the system is 220 nm [39]. As a result, the thermal conductivity calculated using NEMD is smaller than that of GKEMD (see details below). The size of the system used to simulate the ballistic transport of cSi is 2 nm.

D. Calculations of Debye temperature

The Debye temperature for a monatomic crystal is defined as [21]

$$T_{\text{Debye}} = \frac{\hbar}{k_b} v_g (6\pi^2 \rho_N)^{1/3}, \tag{5}$$

where v_g is the group velocity and ρ_N is the atomic number density. Here, we apply Eq. (5) to calculate the Debye temperature which may overestimate the value while providing a safer estimation [21]. The group velocity v_g can be obtained by averaging the transverse and longitudinal group velocities and has the form of

$$v_{g,L} = \left[\frac{3(1-2\nu)}{k_s \rho}\right]^{1/2}, \tag{6}$$

$$v_{g,T} = \left[\frac{3(1-2\nu)}{2(1+\nu)k_s \rho}\right]^{1/2}, \tag{7}$$

in which ρ is the density, k_s is the adiabatic compressibility and ν is the Poisson's ratio. Poisson's ratio is taken 0.3 in our paper as suggested by Huang *et al.* [21]. The adiabatic compressibility k_s in molecular dynamics can be calculated through

$$k_s = -\frac{1}{V}\left(\frac{\partial V}{\partial P}\right), \tag{8}$$

where P and V are the pressure and volume of the system, respectively.

Figure 3 shows the pressure-volume relation in the adiabatic molecular simulations. The adiabatic compressibility can be then obtained via fitting the molecular dynamics simulations results. Recasting Eqs. (6)–(8) into Eq. (5), we can estimate the Debye temperature is 85 K for ZIF-4 and 84 K for ZIF-62.

III. RESULTS AND DISCUSSION

A. Weak temperature-dependent thermal conductivity

Figure 4 reports the temperature-dependent thermal conductivities of cSi, ZIF-4, and ZIF-62 calculated using GKEMD. The thermal conductivity of cSi shows a typical $1/T$ dependence which stems from dominant umklapp (U) phonon processes [46]. We next move to the temperature-dependent thermal conductivities of ZIF-4 and ZIF-62. We would like to emphasize that molecular dynamics simulations may be the only accessible approach to compute the thermal transport properties of MOFs due to their super large unit cells. Our results show that the thermal conductivity of both ZIF-4 and ZIF-62 follow a weak temperature dependence, which agrees with experimental observations well. However, our calculated results of ZIF-4 and ZIF-62 are much higher than measured thermal conductivities [47]. These differences can be addressed from several aspects: (i) the structures of ZIF-4 and ZIF-62 in our simulations are fully symmetric, while the experimental samples possess some moiety sites of partial occupancy which can scatter the lattice vibrations; (ii) there are defects and air entrapment in the samples while molecular dynamics simulates the ideal structures; (iii) the errors stemming from the atomic potentials and the process of the measurements; (iv) bulk crystals in our calculations while small crystals separated by voids in the experiments. It is noted that the assumption of all vibrations [48] occupied in molecular dynamics simulations will not affect our calculated thermal conductivities of ZIF-4 and ZIF-62 since the Debye temperatures of ZIF-4 and ZIF-62 are much lower than the

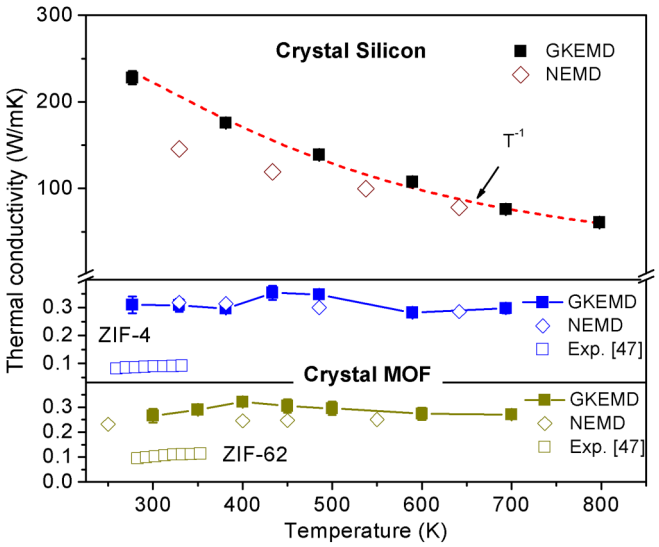

FIG. 4. The temperature-dependent thermal conductivity of crystalline silicon (upper panel), crystal ZIF-4 (middle panel), and ZIF-62 (lower panel) calculated using Green-Kubo equilibrium molecular dynamics (GKEMD) and nonequilibrium molecular dynamics (NEMD). The measurements of ZIF-4 and ZIF-62 are taken from Ref. [47].

simulated temperatures. Meanwhile, although their thermal conductivities show weak temperature dependence which is similar to that of amorphous materials, we would like to emphasize that both ZIF-4 and ZIF-62 are crystals. Therefore, the typical features of the glasslike structures, such as the density of state of ZIF-4 and ZIF-62 becoming smoother, are not observed in our results (see the density of state of ZIF-4 and ZIF-62 below for details). The underlying mechanisms leading to the different temperature dependence of thermal conductivities between ZIF-4, ZIF-62, and the traditional crystalline Si will be analyzed through the comparison of the corresponding vibrational properties and be discussed in detail below. We also calculate the thermal conductivity of ZIF-4, ZIF-62, and cSi using NEMD. For ZIF-4 and ZIF-62, the thermal conductivity calculated using NEMD is similar to that computed using GKEMD (Fig. 4) since the corresponding MFP is smaller than the size of the system (see details below). However, the thermal conductivity of cSi calculated using NEMD is smaller than the value of GKEMD (Fig. 4), which is because the MFP longer than the size of the system (220 nm) is excluded in our NMED results (see details below).

B. Vibrational mean free path

Our spectrum results calculated using the spectral heat current analysis in the frame of NEMD simulations [Fig. 5(a)] show that the maximum MFP of cSi can be as large as several hundreds of nanometers at 350 K, and decreases with temperature due to the stronger U scatterings, e.g., from 215 nm at 350 K to 195 nm at 650 K. However, for ZIF-4 [Fig. 5(b)] and ZIF-62 [Fig. 5(c)], MFPs are found to be quite small, and the MFP spectrum distribution is not largely changed by temperature. In ZIF-4 and ZIF-62, the inherent scatterings among

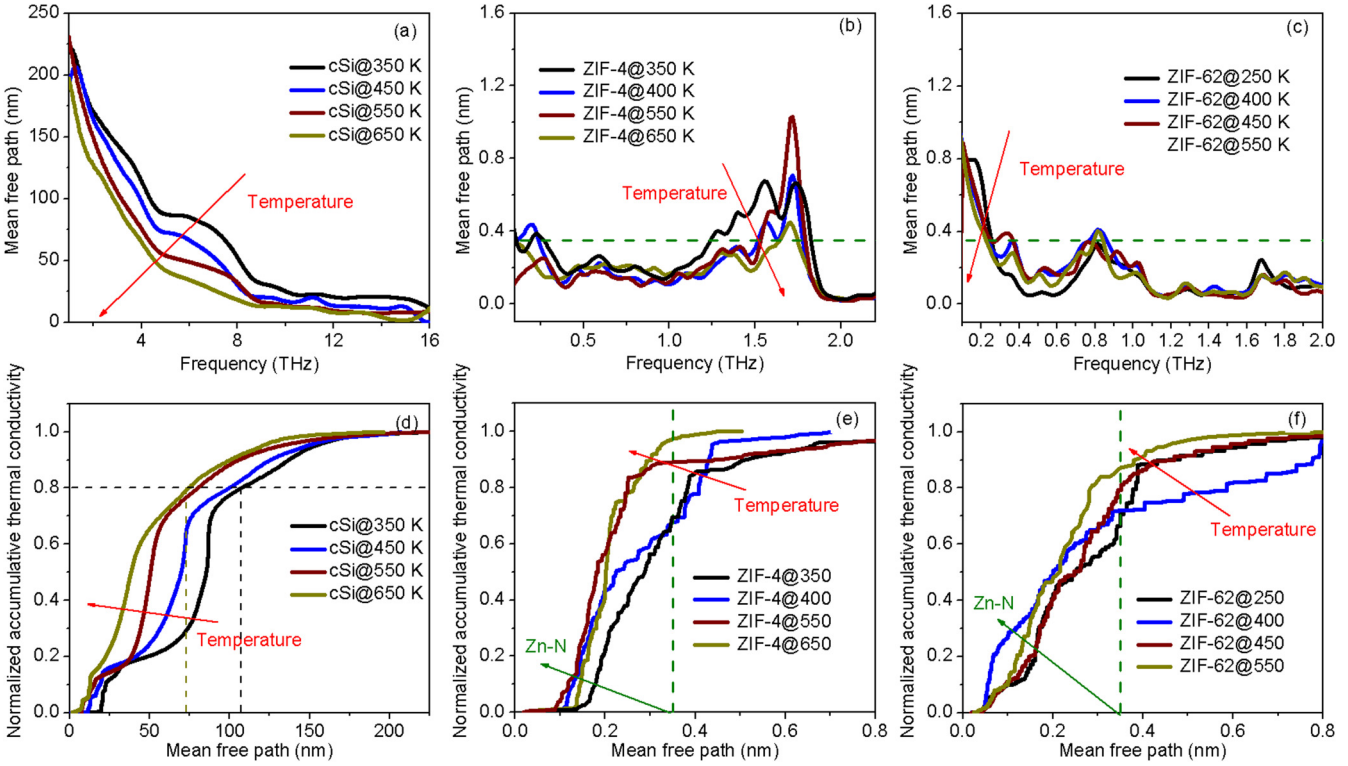

FIG. 5. The mean free path spectrum of (a) crystal silicon, (b) ZIF-4, and (c) ZIF-62 at different temperatures, and the accumulative thermal conductivity of (d) crystalline silicon, (d) ZIF-4, and (f) ZIF-62 at the corresponding temperatures mentioned above. The dashed lines are eye guidance.

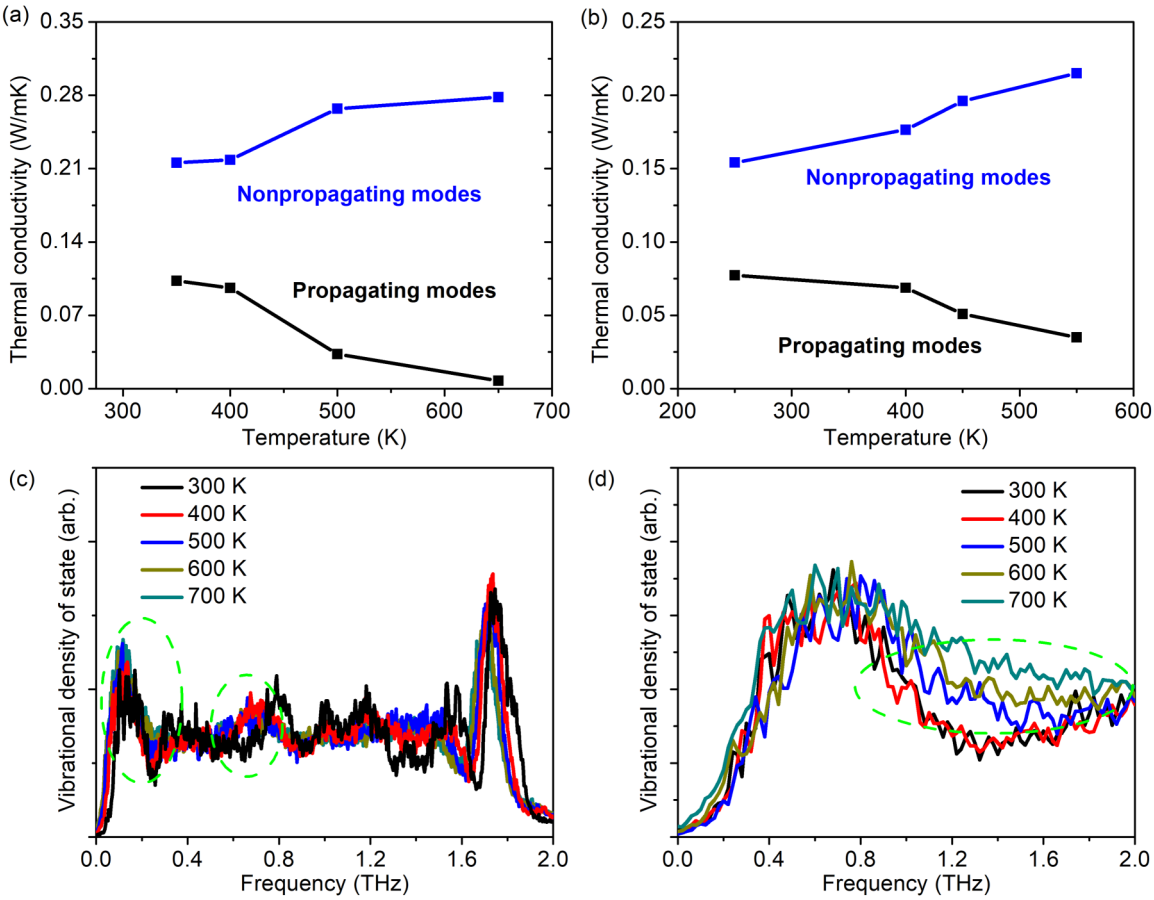

FIG. 6. The temperature-dependent thermal conductivity of propagating vibrational modes and nonpropagating vibrational modes of (a) ZIF-4 and (b) ZIF-62. The vibrational density of the state of Zn and N atoms of (c) ZIF-4 and (d) ZIF-62 at various temperatures.

the vibrations are quite strong due to the large mass difference between organic and metal sites [49,50], and thus the MFPs are found to be short [Figs. 5(b) and 5(c)], which leads to the low thermal conductivity (Fig. 4). It is not surprising to find that the vibrations with frequencies smaller than about 2 THz are the main heat carriers in ZIF-4 and ZIF-62. In solids, high-frequency vibrations normally contribute much less to the heat exchange compared to the low-frequency ones due to their larger scattering rates and flatter dispersions. Meanwhile, it is interesting to find there is a peak at 1.7 THz existing in the mean free path spectrum [Fig. 5(b)]. It is worth noting that the heat current spectrum analysis in the frame of NEMD is frequency dependent rather than mode dependent. Therefore, the mean free path at a specific frequency includes the contributions from all polarizations, which indicates that the mean free path spectrum calculated using spectral heat current analysis in the frame of NEMD is strongly related to the activated modes. As shown in Fig. 6, the vibrational density of states of Zn and N atoms in ZIF-4 displays a peak at 1.7 THz and at all the temperatures, which could be the reason for the peak at 1.7 THz in the mean free path spectra. We also find that the highest peak is found at about 1.7 THz in the MFP spectrum at 550 K for ZIF-4 compared to that at other temperatures [Fig. 5(b)]. Using ReaxFF atomistic simulations, Yang *et al.* [29] find that Zn in ZIF-4 remains fourfold coordinated up to around 550 K and threefold-coordinated Zn appears when the temperature is higher than around 550 K. The highest peak at about 1.7 THz in the mean free path spectrum at 550 K may be due to the sudden appearance of threefold-coordinated Zn in ZIF-4. Furthermore, the vibrational density of states of Zn and N atoms at 1.7 THz first increases from 300 to 400 K and then decreases (see Fig. 6), which may also cause this abnormal transition.

To further characterize the contribution of various heat carriers in the systems, the thermal conductivity accumulation function $\kappa(\Lambda)$ of vibrational modes has been computed from the MFP Λ using

$$\kappa(\Lambda_0) = \sum_{\Lambda<\Lambda_0} \kappa(\Lambda). \tag{9}$$

Our results [Fig. 5(d)] show that the MFP of the vibrations contributed to the thermal conductivity in cSi is broad, i.e., from 10 nm to 1 μm, and decreases with temperature due to the enhanced scattering among heat carriers, while for ZIF-4 [Fig. 5(e)] and ZIF-62 [Fig. 5(f)], the MFP of the vibrations is smaller and ranges from 0.1 to 0.6 nm because of the strong scatterings among these vibrations. Furthermore, we want to emphasize that the vibrations are scattered strongly when they transfer thermal energy from the organic sites to metal atoms rather than stating that the vibrations are localized around the Zn-N bonds.

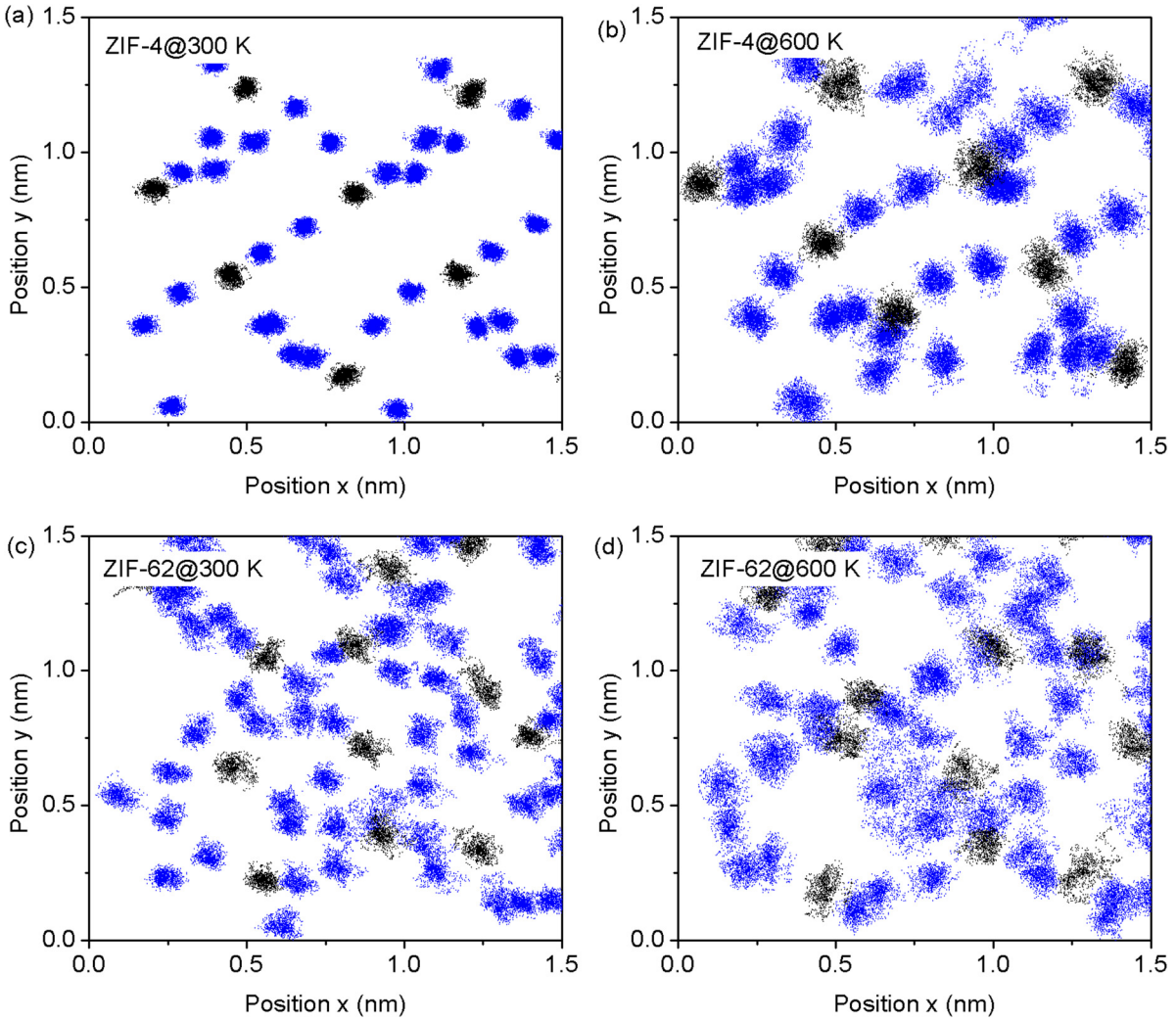

FIG. 7. The trajectories of Zn (black) and N (blue) atoms of ZIF-4 at (a) 300 K, (b) 600 K, and ZIF-62 at (c) 300 K and (d) 600 K.

C. Temperature dependence of various heat carriers

We now characterize the thermal energy carried by different heat carriers. For cSi, all the heat carriers have MFP larger than the minimal interatomic distance of 0.24 nm and therefore can be regarded as propagating vibrational modes [Fig. 5(d)], i.e., phonons. For ZIF-4 and ZIF-62, the distance between Zn and the center of the organic site by simplifying the ZIFs using coarse-grain models, i.e., 0.35 nm, is used as the minimal interatomic distance. We emphasize that the bonds connecting Zn and organic groups are critical for the thermal energy exchange in ZIF-4 and ZIF-62 as they connect the vibrations between the organic sites and those of the metal atom. The vibrational modes with MFPs smaller than 0.35 nm [green dashed line in Figs. 5(e) and 5(f)], may be regarded as diffusonlike vibrational modes since they do not propagate far enough to sample the periodicity of the medium [51]. For ZIF-4 and ZIF-62, both propagating and nonpropagating vibrational modes, i.e., propagons and diffusons, exist and contribute largely to the thermal conductivity [Figs. 5(e), 5(f), and 6] at low temperatures. The thermal conductivity of ZIF-4 and ZIF-62 contributed from the propagating vibrational modes is small compared to that of the conventional crystals, which is because of the strong scatterings among the propagating vibrations due to large mass difference between metal atoms and organic sites [49,50] and the large diffusion of organic sites [52–54]. Meanwhile, the thermal conductivity contributed by the propagating vibrational modes in ZIF-4 and ZIF-62 is found to decrease with temperature [Figs. 6(a) and 6(b)] due to the enhanced scatterings among the vibrations. However, unlike temperature-independent diffusons [51], the thermal conductivity contributed by the nonpropagating vibrational modes in ZIF-4 and ZIF-62, are found to moderately increase with temperature [Figs. 6(a) and 6(b)]. It is known that the nonpropagating vibrational modes are coming from the thermal coupling between different vibrational modes based on their frequencies and overlap of eigenvectors or atomic displacements [45,51]. As shown in Fig. 7, the diffusion of N and Zn is increasing with temperature. The larger diffusion of N and Zn enhances the overlap in the VDOS between Zn and N atoms in the frequency region of which the vibrations are characterized as nonpropagating modes, e.g., the VDOS in 0.2–0.3 and 0.5–0.8 THz for ZIF-4 and the VDOS in 1.0–2.0 THz for ZIF-62 [Figs. 6(c) and 6(d)]. As a result, the thermal conductivity contributed from the diffusons in ZIF-4 (ZIF-62) may increase with temperature

when these nonpropagating vibrations in 0.2–0.3 and 0.5–0.8 THz (1.0–2.0 THz) transfer more thermal energy than the rest of the nonpropagating vibrations. Such a phenomenon has been also observed in superionic systems [55,56]. The temperature-independent thermal conductivity of ZIF-4 and ZIF-62 is then because of the similar variation (increasing or decreasing) rates of the thermal conductivities contributed from the propagating and nonpropagating vibrational modes. For instance, unlike our calculated thermal conductivities of ZIF-4 and ZIF-62 being insensitive to the temperature, the thermal conductivity of MOF-5 shows a weakly positive temperature dependence [21] which may be stemming from the larger variation rate of the thermal conductivity contributed from the nonpropagating vibrational modes compared to that of the thermal conductivity contributed from the propagating vibrational modes. For another example, the thermal conductivity of MOF-74 is found to decrease with temperature when only the propagating vibrational modes are included [57].

IV. CONCLUSIONS

In conclusion, by performing ReaxFF atomistic simulations and spectral heat current analysis, we show that the weak temperature-dependent thermal conductivity in ZIF-4 and ZIF-62 results from the strong scattering among vibrations. This strong scattering among vibrations is stemming from the large mass difference between the metal atoms and the organic sites and the large diffusion of the organic sites. Meanwhile, both propagating and nonpropagating vibrational modes are existing in ZIF-4 and ZIF-62. The thermal conductivities contributed by nonpropagating or propagating vibrational modes in ZIF-4 and ZIF-62 show weak temperature dependence. The similar variation (increasing or decreasing) rates of the thermal conductivities contributed from the propagating and nonpropagating vibrational modes eventually leads to a temperature-independent thermal conductivity of ZIF-4 and ZIF-62. Our results here support a quantitative picture of the weak temperature dependence of the thermal conductivity observed in ZIF-4 and ZIF-62, which may guide the design of future thermal-related applications.

ACKNOWLEDGMENTS

Y.Z. acknowledges the Startup Fund (Grants No. REC20EGR14 and No. a/c-R9246), HKUST-GZU Joint Research Collaboration Fund (Grant No. GZU21EG06), Bridge Gap Fund (Grant No. BGF.008.2021), and SJTU-HKUST Joint Research Collaboration Fund (Grant No. SJTU21EG09) from Hong Kong University of Science and Technology (HKUST). Y.Z. gratefully acknowledges Professor Z. Li (The Hong Kong University of Science and Technology) for proofreading the manuscript.

The authors declare no competing financial interests.

[1] H. Li, M. Eddaoudi, M. O'Keeffe, and O. M. Yaghi, Nature (London) **402**, 276 (1999).
[2] M. Eddaoudi, J. Kim, N. Rosi, D. Vodak, J. Wachter, M. O'Keeffe, and O. M. Yaghi, Science. **295**, 469 (2002).
[3] O. M. Yaghi, M. O'Keeffe, N. W. Ockwig, H. K. Chae, M. Eddaoudi, and J. Kim, Nature (London) **423**, 705 (2003).
[4] J. L. C. Rowsell and O. M. Yaghi, Microporous Mesoporous Mater. **73**, 3 (2004).
[5] N. L. Rosi, J. Eckert, M. Eddaoudi, D. T. Vodak, J. Kim, M. O'Keeffe, and O. M. Yaghi, Science **300**, 1127 (2003).
[6] J. L. C. Rowsell, E. C. Spencer, J. Eckert, J. A. K. Howard, and O. M. Yaghi, Science **309**, 1350 (2005).
[7] J. Y. Lee, O. K. Farha, J. Roberts, K. A. Scheidt, S. T. Nguyen, and J. T. Hupp, Chem. Soc. Rev. **38**, 1450 (2009) .
[8] J. Xiao, T. Zhou, P. Bénard, and R. Chahine, J. Renew. Sustain. Energy **5**, 021415 (2013).
[9] H. Babaei, A. J. H. McGaughey, and C. E. Wilmer, ACS Appl. Mater. Interfaces **10**, 2400 (2018).
[10] M. Woellner, S. Hausdorf, N. Klein, P. Mueller, M. W. Smith, and S. Kaskel, Adv. Mater. **30**, 1704679 (2018).
[11] H. Wang, W. P. Lustig, and J. Li, Chem. Soc. Rev. **47**, 4729 (2018).
[12] H. Li, L. Li, R.-B. Lin, W. Zhou, Z. Zhang, S. Xiang, and B. Chen, EnergyChem **1**, 100006 (2019).
[13] H. Babaei and C. E. Wilmer, Phys. Rev. Lett. **116**, 025902 (2016).
[14] Y. Zhou, B. Huang, and B.-Y. Cao, Mater. Today Phys. **21**, 100516 (2021).
[15] H. Kim, S. Yang, S. R. Rao, S. Narayanan, E. A. Kapustin, H. Furukawa, A. S. Umans, O. M. Yaghi, and E. N. Wang, Science **356**, 430 (2017).
[16] M. J. Kalmutzki, C. S. Diercks, and O. M. Yaghi, Adv. Mater. **30**, 1704304 (2018).
[17] K. B. Sezginel, P. A. Asinger, H. Babaei, and C. E. Wilmer, Chem. Mater. **30**, 2281 (2018).
[18] S. Cui, M. Qin, A. Marandi, V. Steggles, S. Wang, X. Feng, F. Nouar, and C. Serre, Sci. Rep. **8**, 15284 (2018).
[19] L. Han, M. Budge, and P. Alex Greaney, Comput. Mater. Sci. **94**, 292 (2014).
[20] X. Zhang and J. Jiang, J. Phys. Chem. C **117**, 18441 (2013).
[21] B. L. Huang, A. J. H. McGaughey, and M. Kaviany, Int. J. Heat Mass Transfer **50**, 393 (2007).
[22] B. L. Huang, Z. Ni, A. Millward, A. J. H. McGaughey, C. Uher, M. Kaviany, and O. Yaghi, Int. J. Heat Mass Transfer **50**, 405 (2007).
[23] C. J. Glassbernner and G. A. Slack, Phys. Rev. **134**, A1058 (1964).
[24] R. K. Kremer, K. Graf, M. Cardona, G. G. Devyatykh, A. V. Gusev, A. M. Gibin, A. V. Inyushkin, A. N. Taldenkov, and H. J. Pohl, Solid State Commun. **131**, 499 (2004).
[25] G. A. Slack, J. Appl. Phys. **35**, 3460 (1964).
[26] D. G. Cahill, S. K. Watson, and R. O. Pohl, Phys. Rev. B **46**, 6131 (1992).
[27] S. Graulis, D. Chateigner, R. T. Downs, A. F. T. Yokochi, M. Quirós, L. Lutterotti, E. Manakova, J. Butkus, P. Moeck, and A. Le Bail, J. Appl. Crystallogr. **42**, 726 (2009).
[28] R. Gaillac, P. Pullumbi, K. A. Beyer, K. Chapman, D. A. Keen, T. D. Bennett, and F. X. Coudert, Nat. Mater. **16**, 1149 (2017).
[29] Y. Yang, Y. K. Shin, S. Li, T. D. Bennett, A. C. T. Van Duin, and J. C. Mauro, J. Phys. Chem. B **122**, 9616 (2018).
[30] G. Opletal, T. C. Petersen, S. P. Russo, and A. S. Barnard, J. Phys. Mater. **1**, 016002 (2018).

[31] P. K. Schelling, S. R. Phillpot, and P. Keblinski, Phys. Rev. B **65**, 144306 (2002).
[32] J. Tersoff, Phys. Rev. B **39**, 5566 (1989).
[33] R. J. Hardy, Phys. Rev. **132**, 168 (1963).
[34] R. Kubo, J. Phys. Soc. Jpn. **12**, 570 (1957).
[35] S. Plimpton, J. Comput. Phys. **117**, 1 (1995).
[36] F. Müller-Plathe, J. Chem. Phys. **106**, 6082 (1997).
[37] Y. Zhou and M. Hu, Phys. Rev. B **95**, 115313 (2017).
[38] Y. Zhou and M. Hu, Phys. Rev. B **92**, 195205 (2015).
[39] Y. Zhou, X. Zhang, and M. Hu, Phys. Rev. B **92**, 195204 (2015).
[40] K. Sääskilahti, J. Oksanen, J. Tulkki, and S. Volz, Phys. Rev. B **90**, 134312 (2014).
[41] K. Sääskilahti, J. Oksanen, S. Volz, and J. Tulkki, Phys. Rev. B **91**, 115426 (2015).
[42] J. Wang and J. S. Wang, Appl. Phys. Lett. **88**, 111909 (2006).
[43] Y. Sun, Y. Zhou, M. Hu, G. Jeffrey Snyder, B. Xu, and W. Liu, J. Appl. Phys. **129**, 055103 (2021).
[44] Y. Sun, Y. Zhou, J. Han, W. Liu, C. Nan, Y. Lin, M. Hu, and B. Xu, Npj Comput. Mater. **5**, 97 (2019).
[45] J. M. Larkin and A. J. H. McGaughey, Phys. Rev. B **89**, 144303 (2014).
[46] D. A. Broido, A. Ward, and N. Mingo, Phys. Rev. B **72**, 014308 (2005).
[47] S. S. Sørensen, M. B. Østergaard, M. Stepniewska, H. Johra, Y. Yue, and M. M. Smedskjaer, ACS Appl. Mater. Interfaces **12**, 18893 (2020).
[48] Y. Zhou, J. Appl. Phys. **129**, 235104 (2021).
[49] X. Yan, W. Liu, H. Wang, S. Chen, J. Shiomi, K. Esfarjani, H. Wang, D. Wang, G. Chen, and Z. Ren, Energy Environ. Sci. **5**, 7543 (2012).
[50] M. An, L. Li, S. Hu, Z. Ding, X. Yu, B. Demir, N. Yang, W. Ma, and X. Zhang, Carbon **162**, 202 (2020).
[51] P. B. Allen and J. L. Feldman, Phys. Rev. B **48**, 12581 (1993).
[52] W. Qiu, L. Xi, P. Wei, X. Ke, J. Yang, and W. Zhang, Proc. Natl. Acad. Sci. USA **111**, 15031 (2014).
[53] H. Kim, S. Ballikaya, H. Chi, J. P. Ahn, K. Ahn, C. Uher, and M. Kaviany, Acta Mater. **86**, 247 (2015).
[54] K. Zhuo, J. Wang, J. Gao, U. Landman, and M. Y. Chou, Phys. Rev. B **102**, 064201 (2020).
[55] Y. Zhou and S. Volz, Phys. Rev. B **103**, 224204 (2021).
[56] Y. Zhou, S. Xiong, X. Zhang, S. Volz, and M. Hu, Nat. Commun. **9**, 4712 (2018).
[57] X. Wang, R. Guo, D. Xu, J. Chuang, M. Kaviany, and B. Huang, J. Phys. Chem. C **119**, 26000 (2015).